Key Points:
- A global observational database for tracking four major heavy-rain storm systems is established for the 2006–2020
- These four storm systems contribute to over 67% of global annual mean precipitation and over 80% of top 1% precipitation extremes
- Climate model short-range hindcasts underestimate the storm-associated precipitation, especially for heavy precipitation extremes

Correspondence to:
W.-Y. Wu,
wu59@llnl.gov

Author Contributions:
Conceptualization: Wen-Ying Wu, Hsi-Yen Ma
Data curation: Wen-Ying Wu, Hsi-Yen Ma, David Conway Lafferty, Zhe Feng
Formal analysis: Wen-Ying Wu, David Conway Lafferty
Funding acquisition: Hsi-Yen Ma
Investigation: Wen-Ying Wu, Hsi-Yen Ma
Methodology: Wen-Ying Wu, Hsi-Yen Ma, David Conway Lafferty, Zhe Feng, Paul Ullrich
Project administration: Hsi-Yen Ma
Software: Wen-Ying Wu, Hsi-Yen Ma, Zhe Feng, Paul Ullrich, Qi Tang, Jean-Christophe Golaz
Supervision: Hsi-Yen Ma
Validation: Wen-Ying Wu, David Conway Lafferty

Assessment of Storm-Associated Precipitation and Its Extremes Using Observational Data Sets and Climate Model Short-Range Hindcasts

Wen-Ying Wu[1] , Hsi-Yen Ma[1] , David Conway Lafferty[1,2] , Zhe Feng[3] , Paul Ullrich[1,4] , Qi Tang[1] , Jean-Christophe Golaz[1] , Daniel Galea[1] , and Hsiang-He Lee[1]

[1]Lawrence Livermore National Laboratory, Livermore, CA, USA, [2]Department of Atmospheric Sciences, University of Illinois, Urbana-Champaign, IL, USA, [3]Atmospheric Sciences and Global Change Division, Pacific Northwest National Laboratory, Richland, WA, USA, [4]Department of Land, Air and Water Resources, University of California, Davis, CA, USA

Abstract Heavy precipitation, often associated with weather phenomena such as tropical cyclones, extratropical cyclones (ETCs), atmospheric rivers (ARs), and mesoscale convective systems (MCSs), can cause significant socio-economic loss. In this study, we apply atmospheric feature trackers to quantify the contributions of these storm types in observational data sets and climate model short-range hindcasts. We generate a global hourly storm data set at 0.25° spatial resolution covering 2006–2020, based on the tracking results from TempestExtremes and Python FLEXible object TRacKeR. Our analyses show that these four storm types account for 67% of global annual mean precipitation and 82% of top 1% precipitation extremes, with MCSs mainly over the tropics, and ARs and ETCs over the midlatitudes. The percentage of precipitation contributions from these storms also show strong seasonality over many geographical locations. We further apply the tracking results to the Energy Exascale Earth System Model (E3SM) short-range hindcasts and evaluate how well these storms are simulated. The evaluation show that E3SM, with ~1° resolution, significantly underestimates storm-associated precipitation totals and extremes, especially for MCSs in the tropics. Our analysis also suggests that model fails to capture the correct mean diurnal phases and amplitude of MCS precipitation. This phenomenon-based approach provides a better understanding of precipitation characteristics and can lead to enhanced model evaluation by revealing underlying problems in model physics related to precipitation processes associated with the heavy-precipitating storms.

Plain Language Summary Earth system models are immensely useful for understanding how the climate system works. However, it is important to recognize that they have limitations including wet or dry precipitation biases caused by complicated factors. On the other hand, different storm types contribute to regional precipitation differently under varying conditions. Attributing precipitation to sourced storm types is a new approach to understanding model precipitation biases. Here we build a new data set to study precipitation from several storm types including tropical cyclones, extratropical cyclones, atmospheric rivers, and mesoscales convection systems. We find that these four storm types explain 67% of global mean precipitation and 82% of extreme precipitation. We also demonstrate the application of this tool for understanding biases in modeled precipitation. The future application of this new tool will shed light on the causes of modeled precipitation biases and underlying model problems.

1. Introduction

Precipitation is a critical factor for sustaining ecosystems and providing necessary water resources for human use. However, heavy precipitation can cause large socio-economic damages in part due to flooding, crop damages, and landslides. For example, a series of atmospheric river (AR) caused record-high snowfall and rainfall, which further induced severe flooding, mudslides, and power outages in California, U.S. during the winter of 2022–2023 (NOAA National Centers for Environmental Information, 2023). Given that most of disastrous weather events are associated with heavy-rain storms, a crucial ongoing research challenge is to better understand these storm systems and ensure that Earth system models (ESMs) can realistically predict their associated precipitation across a variety of spatial and temporal scales. This information is also important for developing innovative solutions to ensure that infrastructure is resilient to extreme weather events and hydrological changes in a warmer climate.

Visualization: Wen-Ying Wu, David Conway Lafferty
Writing – original draft: Wen-Ying Wu, Hsi-Yen Ma
Writing – review & editing: Hsi-Yen Ma, David Conway Lafferty, Zhe Feng, Paul Ullrich, Qi Tang, Jean-Christophe Golaz, Daniel Galea, Hsiang-He Lee

Unfortunately, it remains challenging for conventional ESMs to realistically simulate the magnitude and timing of these extreme precipitation events (e.g., Kooperman et al., 2022), which are associated with a variety of storm types, for reasons that include biases in model parameterizations and insufficient spatial resolutions (Dai, 2006; Sun et al., 2006). Recently, ESMs with higher spatial resolutions, such as global storm-resolving models, have made significant progress in capturing finer-scale precipitation features (H.-Y. Ma et al., 2022; Stevens et al., 2019). Although higher resolution ESMs, like GSRMs, can better simulate finer-scale structure of storm systems, lower resolution (∼100 km) ESMs are essential and commonly used for exploring long-term Earth system variability and changes with much lower computational cost. It remains worthwhile to diagnose the causes of lower-resolution ESMs precipitation biases from a phenomena-based perspective (Kooperman et al., 2022; Leung et al., 2022).

Previous phenomena-based evaluation of ESMs focused on weather features, including tropical cyclones (TCs), extratropical cyclones (ETCs), ARs and, more recently, mesoscale convective systems (MCSs) (e.g., Caldwell et al., 2019; Feng, Leung, et al., 2021; Feng, Song, et al., 2021; Feng et al., 2023; Leung et al., 2022; Reed et al., 2023; Zarzycki et al., 2017, 2021; Zhao, 2020; Zhao et al., 2009). While early studies usually focused on a single storm type, recent research has begun to analyze multiple storm types simultaneously, such as the works by Zhao (2022), Prein et al. (2023), and Reed et al. (2023). Zhao (2022) used observational data sets and a high-resolution climate model to quantify precipitation from tropical storms, ARs, and MCSs, which are tracked at 6-hourly and 50-km resolution. Prein et al. (2023) used reanalysis to reconstruct historical TCs, ETCs, anticyclones, ARs, MCSs, and frontal systems at hourly and 30-km resolution and highlighted the importance of these storm types and their interactions to extreme precipitation. Reed et al. (2023) evaluated modeled precipitation over the continental US, focusing on TCs, ETCs, and MCSs. These phenomena-based studies rely on feature tracking algorithms for detecting weather phenomena, which have been developed and applied to climate model diagnostics (e.g., Prein et al., 2023; Reed et al., 2023; Ullrich & Zarzycki, 2017; Ullrich et al., 2021; Zhao et al., 2009). These studies represent a significant advance in feature tracking applications and enable a more comprehensive analysis of multiple storm types.

Following upon previous research, the objective of this study is to construct a long-term high-resolution global observational database for tracking four major heavy-rain storm systems: TCs, ETCs, ARs, and MCSs. Moreover, we use tracking outputs to develop an evaluation framework for attributing precipitation associated with these major storm types in ESM simulations. In particular, we conduct climate model short-range hindcasts (H.-Y. Ma et al., 2015, 2021) so the storm events in the hindcasts can be directly compared to the same observational tracking results, which has not been studied. We utilize data at hourly resolution and thus include more short-duration rainfall extremes compared to previous studies that used a coarser temporal resolution (e.g., 6-hourly). This also allows us to examine additional precipitation characteristics, such as the diurnal cycle, which has not yet been analyzed in ESM short-range hindcasts. In this paper, we aim to address the following questions: (a) How much global annual mean precipitation is associated with TCs, ETCs, ARs, and MCSs? (b) What are spatiotemporal characteristics of storm-associated precipitation? (c) How well does the Energy Exascale ESM (E3SM) simulate storm-associated precipitation?

This paper is organized as follows. In Section 2, we introduce the tracking method and data sets. In Section 3, we present the results of storm-associated precipitation based on observational data sets, as well as model evaluations. We further discuss the sensitivity of tracking to model resolutions and the co-occurrences of multiple storm types in Section 4. Finally, Section 5 summarizes our findings and presents conclusions.

2. Feature Tracking Methods and Data

In this section, we present our tracking method and input data. The overall procedures of this framework are shown as a flowchart in Figure 1. Table 1 briefly summarizes the tracking thresholds, which are primarily based on previously published tracking algorithms. Observational data sets ("OBS" hereafter), including reanalysis and satellite-based data sets, are used as the inputs for tracking algorithms.

2.1. TempestExtremes

Feature tracking for TCs, ETCs, and ARs is performed using the TempestExtremes software package (Ullrich, 2022; Ullrich et al., 2021; Ullrich & Zarzycki, 2017), which is a powerful and user-friendly tool to detect nodal or areal features in climate data sets.
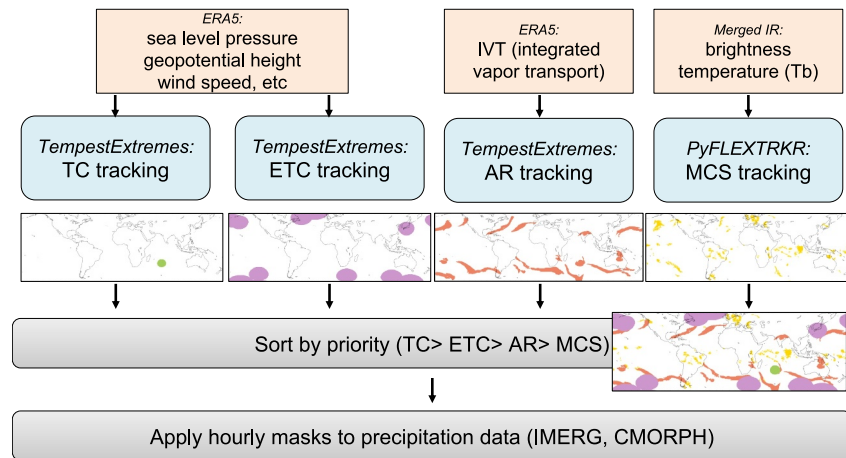
Figure 1. Flowchart of framework in this study. The snapshots represent feature masks for one sample hour. The procedures are conducted for hourly data in 2006–2020.

In this study, the TC detection algorithm employed is based on Zarzycki and Ullrich (2017), where the algorithm thresholds were optimized by comparing with the best available reference from the International Best Track Archive for Climate Stewardship (IBTrACS, Knapp & Kruk, 2010). Here, the TC center is defined as a local sea level pressure minimum with a vertical warm core structure, which is defined by a minimum threshold on geopotential thickness between 300 hPa (Z300) and 500 hPa (Z500). Following Ullrich et al. (2021) and Stansfield et al. (2020), the TC areas are then defined within the radius where the azimuthally averaged surface wind speed exceeding 8 m s^{-1} (r8), which is calculated for each TC at each given time step.

The ETC detection algorithm is similar to the one used for TCs but requiring the absence of a warm core structure. ETC regions are defined as a static 12° radius of great circle distance around the ETC center, which is adopted from Zarzycki (2018) and Hawcroft et al. (2012).

The AR detection algorithm is similar to those used in Ullrich et al. (2021) and McClenny et al. (2020), who applied a Laplacian to the integrated vapor transport (IVT) fields to detect the IVT ridges. Following Ullrich et al. (2021), we use a Laplacian threshold of $-20,000$ kg m^{-2} s^{-1} deg^{-2}. Since this threshold is less restrictive than some studies (e.g., McClenny et al., 2020), we also apply an additional absolute 250 kg m^{-2} s^{-1} IVT threshold. Figure S1 in Supporting Information S1 presents all the TempestExtremes command lines used in this study.

Table 1
Feature Tracking Algorithms, Parameters, and the Defined Regions for Masking Precipitation

Feature	Primary tracking method	Other threshold	Primary reference
Tropical cyclone (TC)	Center defined by sea-level pressure minima with warm core structures (Z300-Z500); Regions defined by wind speed r8 radius	48 hr minimum lifetime with surface wind > 10 m s-1; altitude < 150 m; lat < 50° N/S; center located in lat < 30°N/S for at least 1 hr	Zarzycki and Ullrich (2017)
Extratropical cyclone (ETC)	Center defined by sea level pressure minima and without warm core structures; Regions defined by 12° great-circle distance (GCD)	48-hr minimum lifetime with altitude < 70 m	Ullrich et al. (2021)
Atmospheric River (AR)	Regions with ridges of integrated vapor transport (IVT): Laplacian of IVT $\leq -20,000$ kg m^{-2} s^{-1} deg^{-2}, and IVT > 250 kg m^{-2} s^{-1}	Area > 400,000 km^2 with at least half grid cells located in lat > 20°N/S	Ullrich et al. (2021)
Mesoscale Convective System (MCS)	Regions of Tb < 241 K with inner core Tb < 225 K	Cloud system area > 40,000 km^2	Feng, Leung, et al. (2021)

2.2. PyFLEXTRKR

We used the global MCS tracking data produced by the Python FLEXible object TRacKeR (PyFLEXTRKR) algorithm (Feng et al., 2018, 2019, 2023; Feng, Leung, et al., 2021; Feng, Song, et al., 2021), which has capabilities to track convective clouds from a variety of OBS and model simulations. MCSs here are identified as cold cloud systems, where brightness temperature (Tb) is less than 241 K with inner cores of Tb less than 225 K. A given MCS system is defined as a cold cloud system >40,000 km^2 continuously for longer than 4 hr. Here we use the tracking results only defined by Tb ("cloudtracknumber") and before the exclusion of TCs and ARs.

The original global PyFLEXTRKR MCS tracking data set is 0.1° and hourly from 2000 to 2020 (Feng, Leung, et al., 2021; Feng, Song, et al., 2021). When a significant fraction of a given satellite hourly scan is missing, no MCS tracking data is produced for that hour. Since the missing Tb scans mainly occur over East Asia during 2003–2005 (Figure S9 in Feng, Leung, et al. (2021) and Feng, Song, et al. (2021)), we only use the data from 2006 and thereafter, and remove those missing hours (621 hr, <0.5% of total hours) from all further analysis. Statistics of data coverage are shown in Figures S1 and S2 in Supporting Information S1.

2.3. Observational and Reanalysis Data Sets

All the required variables (Table 1) for TC, ETC, and AR tracking with TempestExtremes are from the ERA5 reanalysis (Hersbach et al., 2018, 2020). ERA5 is the latest reanalysis from the European Center for Medium-Range Weather Forecasts which applied data assimilation to integrate models and observations to produce the best-estimate historical reconstruction of the seamless fields. We use the hourly and 0.25° data for tracking TCs, ETCs, and ARs.

Since the spatiotemporal scale of MCSs is much finer than TCs, ETCs, and ARs, we find that MCS frequency can be significantly underestimated when tracking on the 0.25° Tb converted from ERA5 outgoing longwave radiations with TempestExtremes. Therefore, we directly use the published PyFLEXTRKR global MCS data set (Feng, Leung, et al., 2021), which uses the National Aeronautics and Space Administration merged geostationary satellite infrared brightness temperature Tb data (Janowiak et al., 2001).

Two satellite-based, high-spatiotemporal-resolution precipitation data sets are used to assess data uncertainties, especially for extreme precipitation. The Integrated Multi-satellitE Retrievals for GPM (IMERG, Huffman et al., 2019) is a gridded precipitation product that combines satellite microwave and infrared precipitation retrievals with monthly rain gauge bias corrections. Here we use IMERG Level 3 Final Run Version 06B at half-hourly and 0.1° resolution, converted and regridded to hourly and 0.25° resolution with area-conservative remapping in Climate Data Operators (CDO, Schulzweida, 2023). The other precipitation product used is NOAA Climate Prediction Center MORPHing technique product (CMORPH, P. Xie et al., 2019), which combines passive microwave measurements. Here we use the hourly CMORPH product at 0.25° resolution. Both IMERG and CMORPH have their limitations including (a) minor incomplete coverage, especially for CMORPH, (b) underestimation of heavy rainfall events and overestimation of light rainfall in IMERG (Ayat et al., 2020; Cui et al., 2020; Derin et al., 2022; Wang et al., 2022), (c) uncertainties and limitations in measurements, algorithms, and calibration (Huffman et al., 2020; P. Xie et al., 2019). To classify rain and no rain hours, we use a threshold of 0.2 mm hr^{-1} for results in Figure 2, which is the criteria used in Huffman et al. (2020). Since CMORPH exhibits more incomplete coverage over high latitudes, we use IMERG for our main OBS results and present the CMORPH results in Supporting Information S1.

2.4. Prioritization of Storm Systems

The four storm types (TC/ETC/AR/MCS) can sometimes co-occur. As our goal is to identify precipitation from individual phenomena and to avoid double counting, we perform a workflow prioritization in the order of TC, ETC, AR, and finally MCS. That is, TC masks with the highest priority are placed before ETC/AR/MCS masks, and ETC/AR overlapping regions are defined as ETC (Figure 1). This ordering is similar to the one in Zhao (2022) and is assigned due to their difference in tracking uncertainties, and the impacts of prioritization to the results are explored in the Discussion. Compared to studies of single-feature tracking, this prioritization results in a lower precipitation contribution from MCSs, since TCs, ETCs, and ARs are already

filtered. Finally, we produce hourly gridded classification data (0: no feature detected, 1: TC, 2: ETC, 3:AR, and 4: MCS), which are then applied to mask the hourly precipitation (Figure 1). Simply, the precipitation within the masks of each storm is treated as precipitation associated with the storm. TC precipitation is precipitation within r8 radius. ETC precipitation is precipitation inside static 12° radius. AR precipitation is within the IVT-detected area, and MCS precipitation is within the Tb-detected area.

In our analysis and figures, we also mask out the dry regions with long-term average precipitation less than 0.5 mm d^{-1} (about 0.02 mm hr^{-1}) from either IMERG or CMORPH, and the regions with substantial missing Tb scans (Figure S2 in Supporting Information S1). The total size of the masked-out regions is 64,756,543 km^2, which consists of 14.6% area in 60°S–60°N.

2.5. E3SM Short-Range Hindcasts

The uniqueness of this study is that we further apply the OBS tracking results to climate model short-range hindcasts with the US Department of Energy's E3SM version 2 at a horizontal resolution ~1° (native ne30pg2 grid, and regridded to 1° × 1°) and with 72 vertical levels (Golaz et al., 2022; S. Xie et al., 2019). Two-day long hindcasts are initialized every day at 00Z with ERA5 state variables for the entire 2011 following the procedure in H.-Y. Ma et al. (2015, 2021). We only conduct simulation for 1 year due to computational cost. Also, H.-Y. Ma et al. (2021) found that differences in precipitation mean errors between individual hindcast years are small and generally not sensitive to interannual variability. The ocean and sea ice components are prescribed with the NOAA optimum interpolation weekly sea surface temperature and sea ice (Reynolds et al., 2002). Day 1 is within the timeframe of initial spinup (H.-Y. Ma et al., 2013). Therefore, we then composite the results of 24–48 hr (Day 2) lead time in 2011. Also, the results do not change much with hindcast lead times beyond 0–24 hr (Day 1). The OBS gridded classification data (storm masks in 0.25°) mentioned above are regridded to 1° × 1° with largest-area-fraction remapping in CDO for matching the model resolutions. In this way, the OBS feature-tracking masks are directly applied to Day 2 hindcasts precipitation.

3. Results

3.1. Climatology From OBS

To understand how often each storm type occurs, we first analyze the frequency of rain hours from IMERG (Figure 2) and CMORPH (Figure S3 in Supporting Information S1). Rain hours are defined when hourly OBS precipitation is larger than 0.2 mm hr^{-1}. Among the four storm types, TC-associated precipitation occurs rarely and is only present in certain ocean basins—the West Pacific, subtropical East Pacific, South Indian, North Atlantic, South Pacific, and North Indian. On average, TCs contribute to 1.4% of rain hours globally (area-averaged over valid regions) with the biggest hotspot being in a few small regions of the East Pacific, with a local contribution up to 33.7% of rain hours. ETCs mostly occur at high latitudes over the ocean and contribute to 14.7% of rain hours (Figure 2b) and 10.4% of total hours globally (Figure S4 in Supporting Information S1). ARs mainly occur in midlatitudes over the storm track regions and contribute to 18.9% of rain hours and 5.1% of total hours globally. MCSs contribute to 16.2% of rain hours globally and most of the rain hours in the tropics, especially over the warm pools, intertropical convergence zone (ITCZ), Africa and major monsoon regions. Contribution from MCSs can also be found in some area in the midlatitudes, such as the US Great Plains, along the lee of Andes, and south Asia. These four storm types account for 51.2% of rain hours and 18.4% of total hours, with the remaining 48.8% rain hours (Figure 2f) arising from other precipitation sources, such as isolated convection cells or weaker versions of these four storm types which fall outside the tracking criteria.

In Figures 3 and 4, we further examine the precipitation amount contributed from these four storm types. The spatial patterns of precipitation amount (Figure 3) largely follow the ones of frequency (Figure 2). The region of largest TC precipitation amount is over the western Pacific (Figure 3a) with gridded values up to 2.82 mm day^{-1}. The largest ETC precipitation regions follow the midlatitude storm tracks with the largest contribution in the northwestern Pacific. Since ARs are generally associated with ETC cold fronts, the distribution of AR precipitation amount approximately follows the ETC distribution (Figures 3b and 3c) and contributes to 20%–60% precipitation within 20–50°S and 20–50°N (Figure 4c). MCS precipitation contribution reaches the highest local values compared to ones from TC/ETC/AR and often exceeds 50% of the total precipitation in the tropics (Figure 4d). This is perhaps unsurprising, as TC/ETC/AR events are largely absent around the equator. The average precipitation contributions from TC/ETC/AR/MCS 60°S–60°N are 2.7%, 15.8%, 21.7%, and 26.7%,
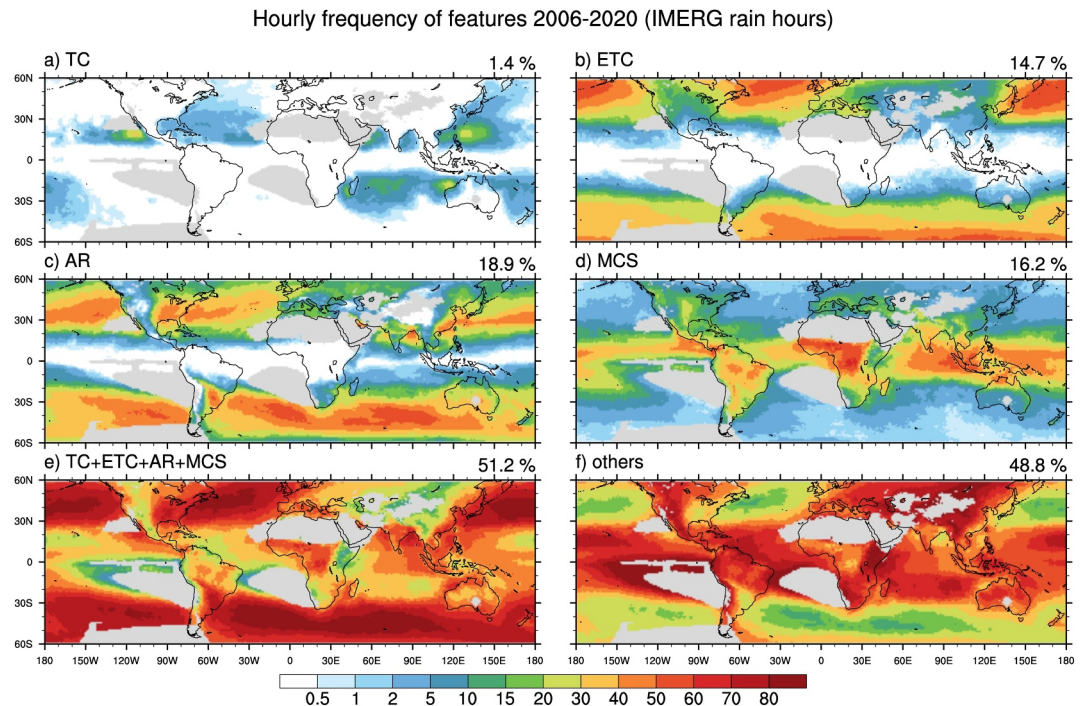
Hourly frequency of features 2006-2020 (IMERG rain hours)

Figure 2. Contribution of each storm type to rain hours, summarized from hourly data in 2006–2020. Rain hours are defined when hourly IMERG precipitation is larger than 0.2 mm hr^{-1}. The upper right numbers are the area-weighted averages over 60°S–60°N excluding the gray regions. Others (f) are other precipitation sources.

respectively. Results from CMORPH are in good consistency (Figure S5 in Supporting Information S1), with attributed precipitation equal to 2.5%, 15.9%, 22.2%, and 23.9%, respectively. Note that these numbers emerge after applying the ordering procedure discussed in Section 2.4. Overall, these four storm types accounts for 66.9% of total precipitation using IMERG and 64.5% using CMORPH.

We further investigate the dominant storm type for precipitation contribution at any given location and in different seasons (Figure 5). The dominant precipitation source is classified as the storm type with the largest precipitation contribution, if its contribution is larger than 25%. If there is no more than 25% of precipitation contributed by any storm type, no dominant storm type is present and is marked in white in Figure 5. Figures 5b–5e show strong seasonality of the dominant storm types in the midlatitudes. TC precipitation only dominates in a small fraction of ocean regions within 15–30°S and 15–30°N. ETCs dominate over ocean in the mid and high latitudes. As expected, precipitation over the west coast of North America and Europe is dominated by ARs in December–February (DJF). In the tropics, MCSs dominate throughout the year. In June–August (JJA), MCSs also dominate over the central US and the South Asian monsoon regions, while in DJF, MCSs also dominate over the South America, South Africa, and the northern part of Australia.

As shown in Figure 5, the dominant storm types are different in different seasons and latitude bands. Here we focus on JJA over three latitude bands to examine the probability density function (PDF) of the hourly precipitation (Figure 6 for IMERG and Figure S6 in Supporting Information S1 for CMORPH). The samples are all hourly data in JJA 2018–2020 across 0.25° grid cells and grouped into log10-scale bins. In all three latitude bands (Figures 6a, 6c, and 6e), these four storm types together contribute to most of the heavier precipitation (>4 mm hr^{-1}), and other precipitation sources contribute to most of the lighter precipitation (<0.1 mm hr^{-1}, Figures 6a, 6c, and 6e). We further decompose individual contributions from each storm type in Figures 6b, 6d, and 6f. Within 0–15°N (Figure 6b), MCSs contribute to most of the precipitation in all bins, with a similar frequency distribution of combined TC/ETC/AR/MCS precipitation shown in Figure 6a (red curve). Within 15–30°N (Figure 6d), ARs and MCSs contribute to most of the precipitation across the distribution, with small contribution from both TCs and ETCs. MCSs contribute to more intense precipitation while ARs have broader distribution, which contribute to both intense and light precipitation. Of the three latitude bands, the distribution
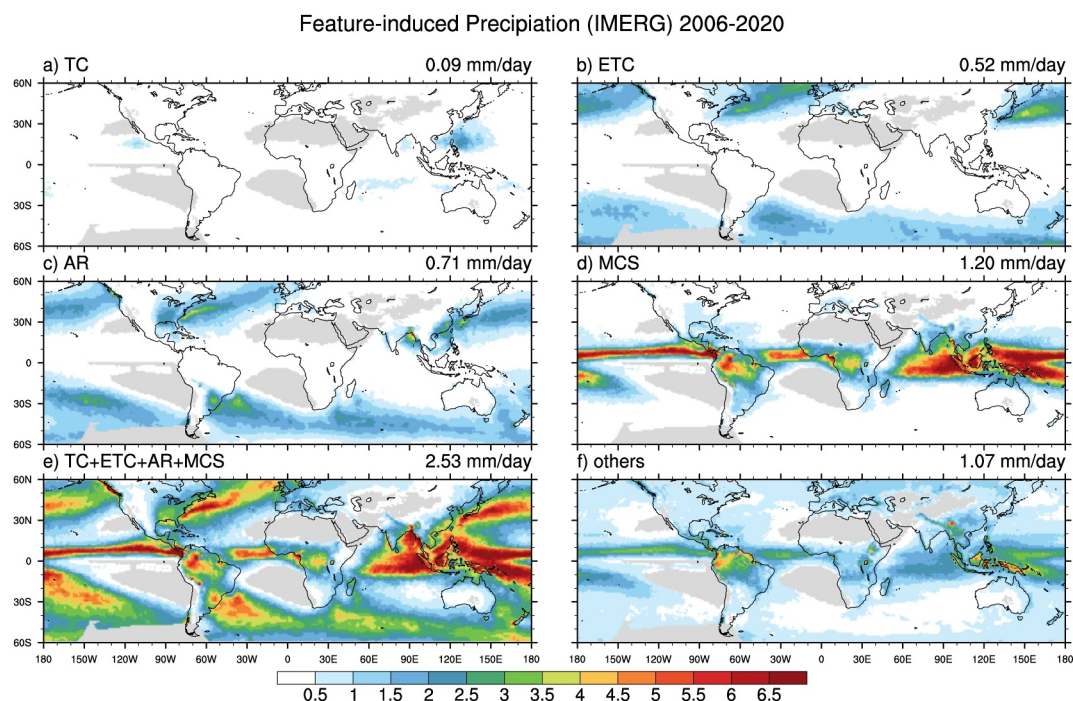
Feature-induced Precipitation (IMERG) 2006-2020

Figure 3. Mean precipitation amount (mm day^{-1}) from each feature based on IMERG for 2006–2020.

of TC precipitation is mostly confined within 15–30°N consistent with the results seen in Figure 5. Within 30–45°N (Figure 6f), precipitation is mostly contributed by ARs and ETCs, with a smaller contribution from MCSs. Overall, these four storm types account for most of the heavy precipitation in all three latitude bands, and MCS particularly contributes to most of the heavy precipitation in low-to-middle latitudes.
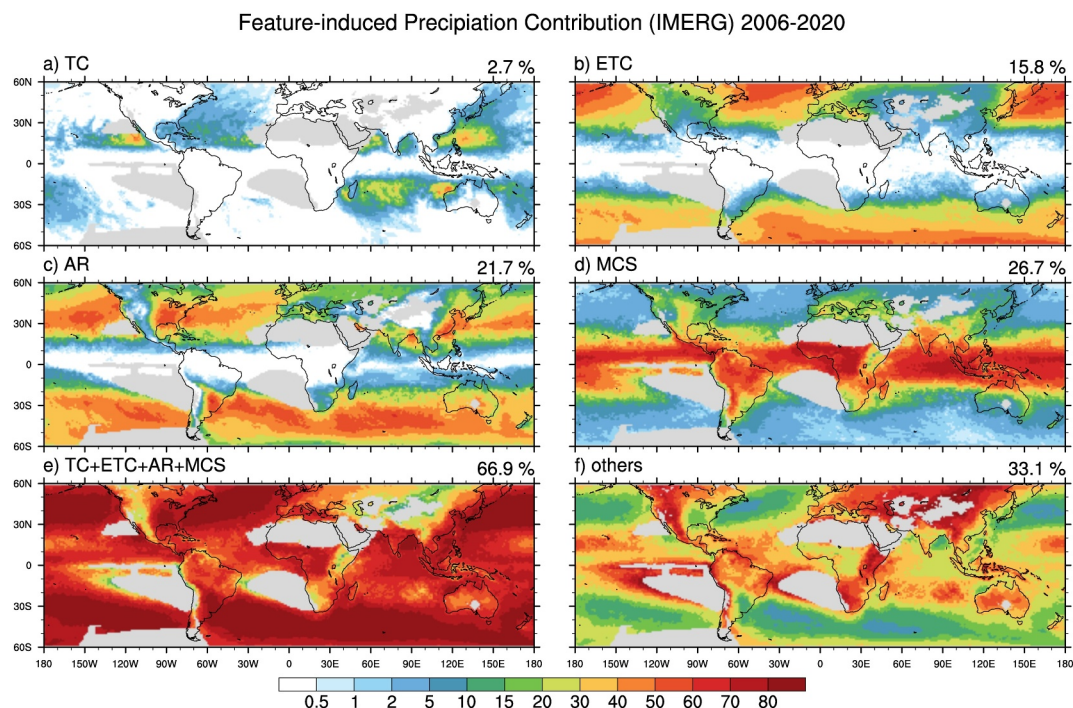
Feature-induced Precipiation Contribution (IMERG) 2006-2020

Figure 4. Precipitation contribution (%, relative to the total precipitation of each grid cell) based on IMERG for 2006–2020.
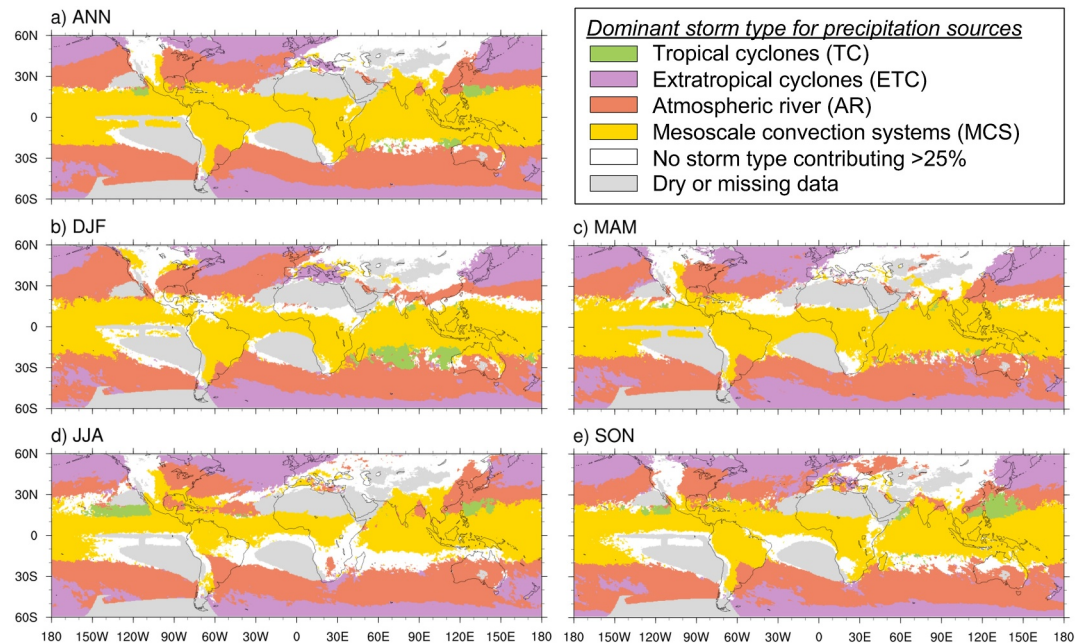
Figure 5. Dominant storm types based on IMERG precipitation in 2006–2020. Colors show the feature with the largest precipitation contribution in each grid cell. If there is no feature that contributes to more than 25% of total precipitation, the regions are marked as white. (a) Annual average across all months (ANN), (b) December–February (DJF), (c) March–May (MAM), (d) June–August (JJA), and (e) September–November (SON). 2017 June is excluded from JJA statistics due to a large portion of missing Tb data.

To further quantify the contribution of precipitation extremes from these four storm types, we present the individual and combined storm precipitation contribution to the top 1% precipitation hours in Figure 7 (IMERG) and Figure S7 in Supporting Information S1 (CMORPH). We first calculate the 99th precipitation amount based on all hourly data (Figure 7f). Then, we analyze the compositions of the accumulated precipitation in top 1% precipitation hours (hourly precipitation greater than the 99th percentile) based on different storm types (Figures 7a–7e). Together, these four storm types explain 81.5% of the extreme precipitation in the global mean and contribute to more than 70% of extreme precipitation in most regions (Figure 7e). Most exceptions occur in the dry regions, where the 99th percentile is generally low (Figure 7f). Overall, the results further confirm that these four storm types account for a substantial proportion of extreme precipitation.

The hourly resolution provides unprecedented opportunities to understand the characteristics of the diurnal cycles and the contributions of each storm type. The hourly precipitation fields, which are associated with different storm types, are composited to the averaged diurnal cycles (24 hr) for each grid cell based on the local standard time. A Fourier analysis is applied to the averaged diurnal cycles. The first Fourier harmonic component is used for the amplitude and timing of diurnal cycle, consistent with methods used in Tao et al. (2022), P. Xie et al. (2019), and S. Xie et al. (2019). Overall, the results in Figure 8 shows that MCS precipitation has pronounced amplitude of diurnal cycle, and therefore dominant patterns of storm precipitation (Figures 8a and 8b). In most regions, the diurnal phase of TCs, ETCs, and ARs are not pronounced (Figure S8 in Supporting Information S1) since the systems are long-lasting, and their precipitation mechanisms are not mainly related to diurnal radiative forcing. A diurnal cycle for ETCs and ARs is only found in some parts of the midlatitude oceans with mild amplitudes and peaks around early morning for ETCs and ARs (Figures S8b and S8c in Supporting Information S1). In contrast, diurnal cycles of tropical MCS precipitation are pronounced with nocturnal to early morning peaks over ocean, and evening peaks over land (Figure 8a), consistent with previous findings (e.g., Nesbitt & Zipser, 2003). The spatial transition of diurnal peaks can also be found along MCS movements, which are usually initiated at the lee of the mountains in the early afternoon and travel downstream (e.g., east of the Rocky Mountains as also shown in Feng et al. (2019), lee of the Andes in South America). Figure 8c shows that land-ocean contrast of diurnal cycle from other precipitation sources are also pronounced. However, earlier peaks are both found over land and ocean (Figure 8c), compared to the phase from storm precipitation (Figure 8b). Nocturnal rainfall occurs in tropical
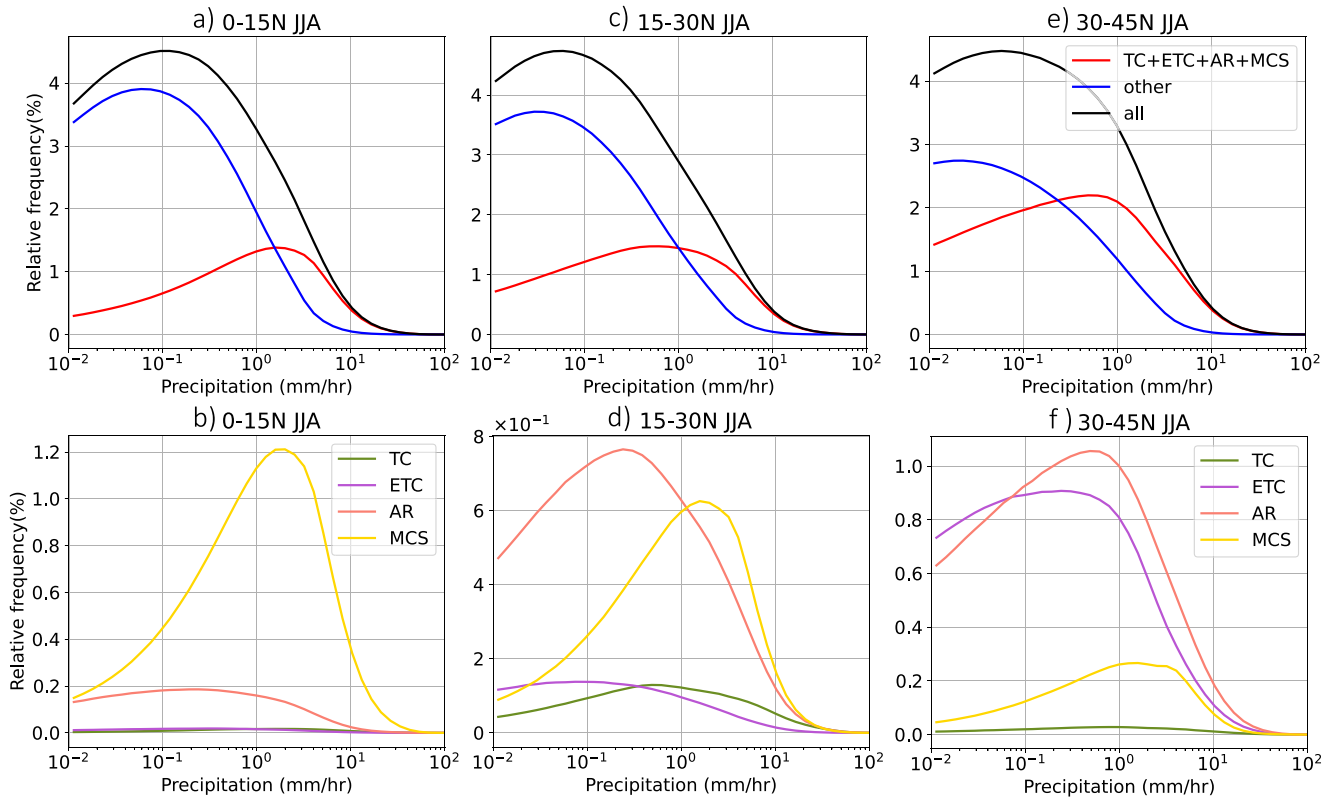
Figure 6. Hourly precipitation (mm hr^{-1}) distribution across time and space for each latitude bands during 2018–2020 JJA using IMERG. Precipitation samples are grouped into 50 log10-scale bins between 0.01 and 1,000 mm hr^{-1}. Relative frequency represents the counts relative to (normalized by) the counts of all precipitation (sample numbers of black lines) in each latitude band. Distributions of all storm types are shown in red, other precipitation sources in blue, and total precipitation in black within (a) 0–15°N, (c) 15–30°N, and (e) 35–45°N. Decompositions of individual storm type in panels (b, d, and f).

oceans and late afternoon rainfall occurs over the land (Figure 8c), implying that the other precipitation sources are likely coming from local convection driven by local thermodynamic instability. The overall diurnal cycle, shown in Figure 8d, has the combined patterns of Figures 8b and 8c. MCSs represent an important driver of the overall diurnal cycle. The results here provide another perspective to understand the diurnal cycle of precipitation and highlight the contribution of MCSs, a key factor in controlling the phase and amplitude of the diurnal cycle of precipitation.

3.2. Evaluation of E3SM Short-Range Hindcasts

One important question we want to address is how well ESMs simulate these storms, as they are critical to understand our current Earth systems and their changes in the future, especially changes related to precipitation. Realistic simulations of precipitation, however, is not trivial as ESMs would require accurate simulations of convection and cloud processes. Furthermore, high-resolution models and different precipitation parameterizations are usually required to better simulate the dynamics and thermodynamics structure of these storm systems (Prein et al., 2021; Shields & Kiehl, 2016; Zarzycki et al., 2017). For free running ESM simulations, such as those simulations from the Phase 6 of Coupled Model Intercomparison Project (CMIP6, Eyring et al., 2016), feature tracking is needed to track these storm systems separately from OBS. Conventional CMIP6 models with typical horizontal resolution of ~100 km, however, are too coarse to adequately represent these storms, especially for TCs and MCSs. Tropical cyclone structure is typically not well resolved for models with grid spacing coarser than 0.5°. And while the fine-scale structures of MCSs are only present at convection-resolving scales, MCS-like features are merely present in some models at 0.25°. Nonetheless, care should be taken under these circumstances when comparing feature statistics from free model runs with OBS. Instead of using free running simulations, we conduct series of short-range 2-day long hindcasts with E3SM for the entirety of 2011. We apply the same observed feature-tracking masks directly to Day 2 (24–48 hr) hindcasts because the hindcasts are initiated
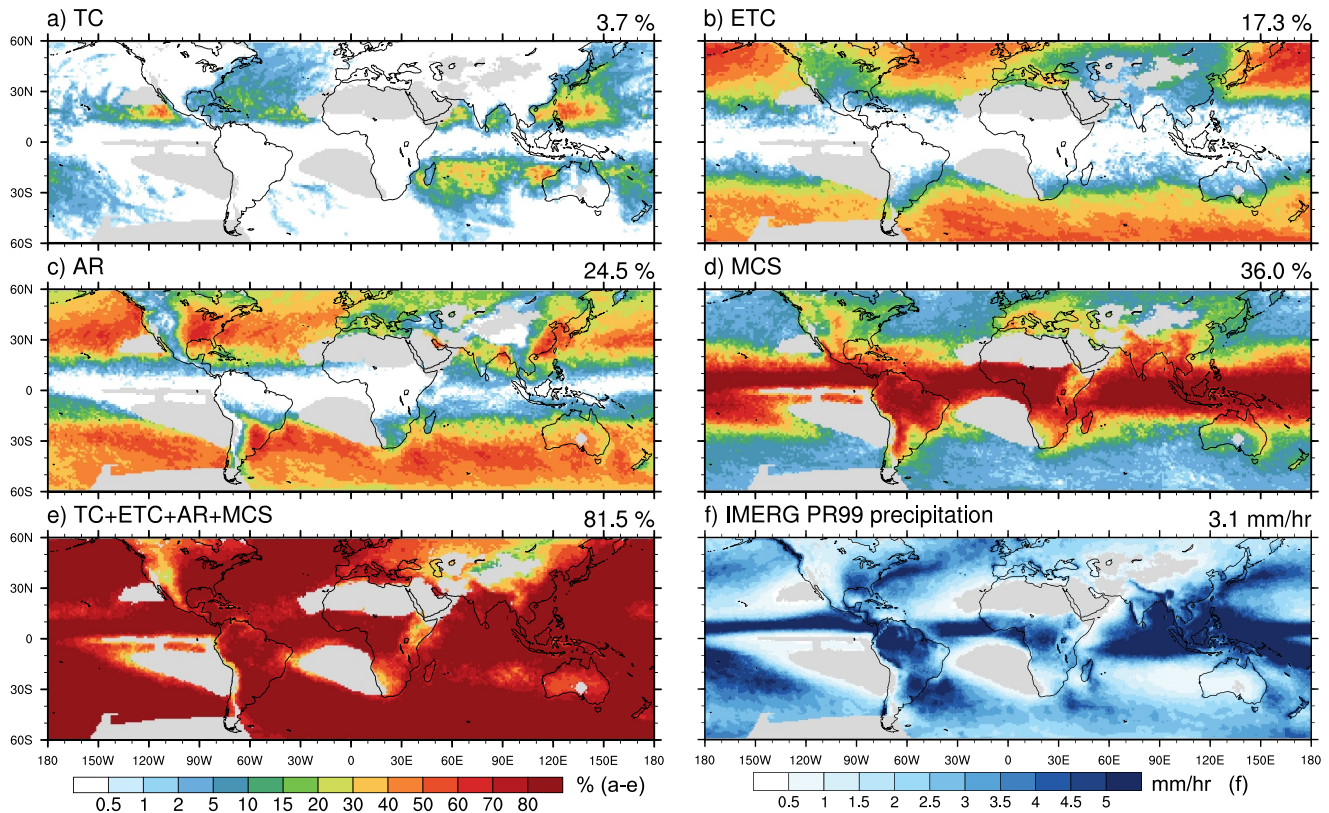
Figure 7. (a–e) Precipitation contribution (%) to top 1% precipitation hours from each storm type. The contribution is defined as the fraction of accumulated precipitation greater than local 99th percentile values (f). 99th percentile values are statistics based on hourly IMERG precipitation during 2006–2020 at 0.25° resolution.

with ERA5 reanalysis and the large-scale environment remains close to ERA5 at Day 2 (H.-Y. Ma et al., 2015). However, it does not necessarily mean model captures all the storms as OBS.

Figures 9a–9c show the 2011 mean precipitation from the Day 2 hindcasts, OBS, and hindcast bias (hindcast-OBS), respectively. Model results show underestimated precipitation over regions such as cores of the ITCZ, the northeasatern Pacific and the north Atlantic, and wet biases over regions such as central Africa and part of the Maritime Continent (Figure 9c). Figures 9d–9i further show precipitation biases from different storm types. We find that the model exhibits underestimated precipitation for all four storm types (Figures 9d–9h) but over-estimated precipitation for other sources (Figure 9i). Of all four storm types, MCS-associated precipitation biases are the main contributor to the underestimation of storm-associated precipitation found in the tropics (Figure 9g), while AR- and ETC-associated precipitation biases are the main contributors in midlatitdues (Figures 9e and 9f). The small portions of overestimated precipitation from storm-associated precipitation are mostly smaller than 0.05 mm hr^{-1}, with a small cluster in the northwestern part of North America from ETCs (Figure 9h).

We further compare the precipitation PDF from OBS and hindcasts in Figure 10. The samples are obtained from hourly precipitation at 1° grids over 60°S–60°N in 2011. Modeled distributions suggest an overall overestimation of light precipitation but underestimation of heavy precipitation (black lines in Figure 10a). Furthermore, the overestimated light precipitation is mostly from other precipitation types while the underestimated heavy pre-cipitation is mostly from storm precipitation (Figure 10a) This explains the underestimation of storm precipi-tation, and overestimation of other precipitation shown in Figures 9h and 9i. The overestimation of light precipitation is a long-standing "frequent drizzle problem" for many GCMs (e.g., Chen et al., 2021), though it had been improved from E3SM v1 to v2 by revised convective triggering function (Golaz et al., 2022; S. Xie et al., 2019). In a recent study (W. Ma et al., 2023), the drizzle problem also been found in reanalysis for AR precipitation, which is consistent with our results.
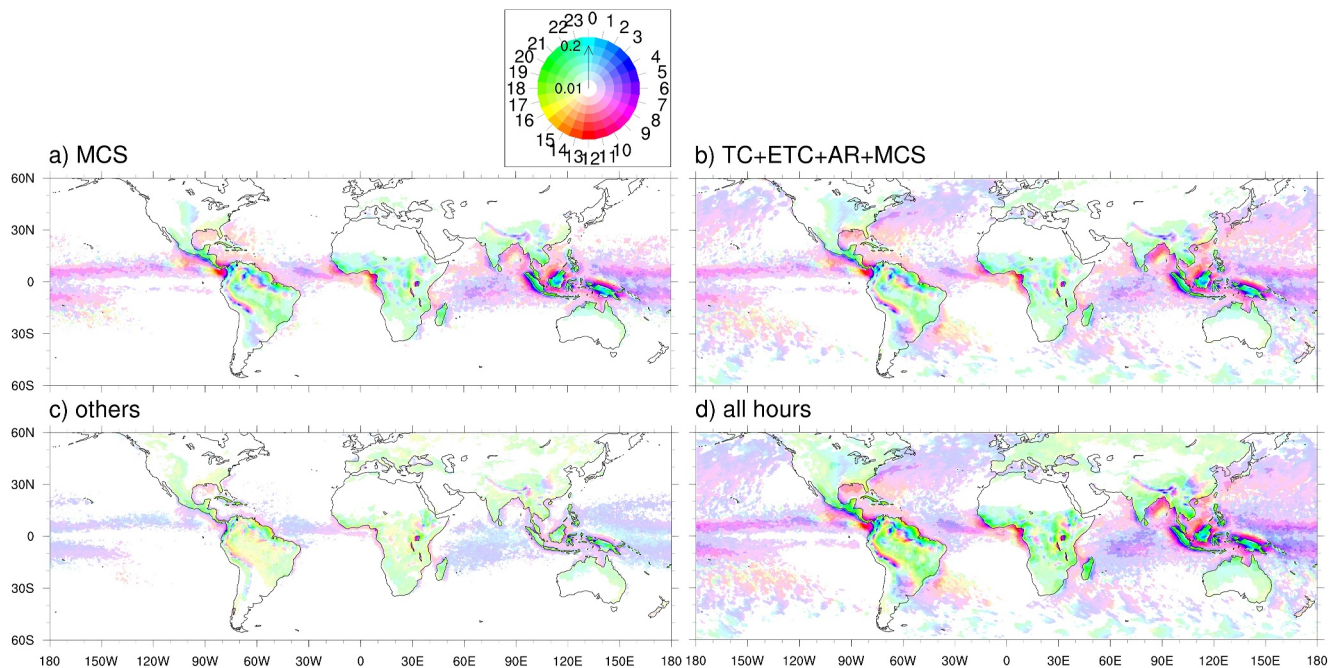
Figure 8. Composited diurnal cycle of IMERG precipitation. The diurnal phase (shown as colors) is in local standard time. The diurnal amplitude in mm hr^{-1} is shown as saturation. Precipitation magnitudes in panel (a–d) are all normalized by all hours used in this study during 2006–2020, not the individual storm event hours. Dry regions, missing area regions, and regions with diurnal amplitude smaller than 0.01 mm hr^{-1} are now shown. Diurnal amplitudes of tropical cyclone, extratropical cyclone, and atmospheric river are relatively small and shown in Figure S8 in Supporting Information S1.

The PDFs also shown that modeled precipitation rarely exceeds 10 mm hr^{-1}. Examining the PDFs of different storm types (Figure 10b) reveals that overestimated light precipitation and underestimated heavy precipitation (>2 mm hr^{-1}) can be found in most of the storm types except for TCs in the model simulations. For TC-associated precipitation, the model produces a narrower distribution compared to OBS with overestimated moderate precipitation (0.2–2 mm hr^{-1}) and underestimated precipitation at both tails. For heavier precipitation, which is
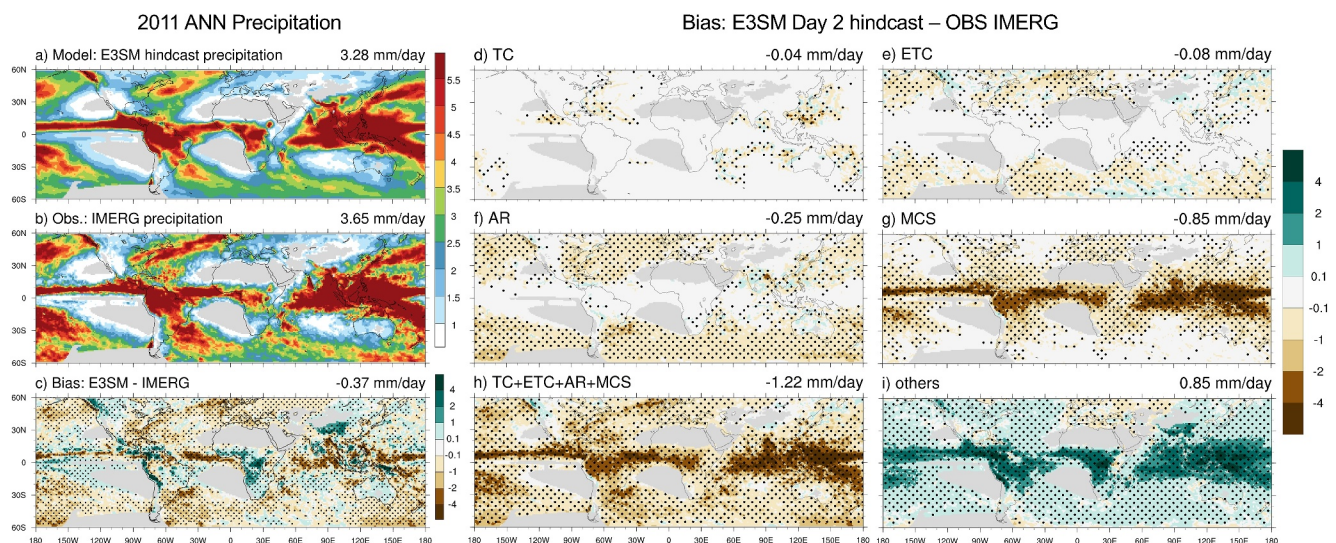

Figure 9. Comparison of modeled and OBS precipitation (mm day^{-1}) in 2011 (a) E3SM hindcast Day 2, (b) IMERG OBS, and (c) their differences (E3SM minus IMERG). Precipitation differences are then classified into tropical cyclone, extratropical cyclone, atmospheric river, mesoscale convective system, and other precipitation sources using the same classification method as in Section 2. Dots mark the regions where there are statistically significant at 95% level determined by a *t*-test using variances of hourly data in 2011.
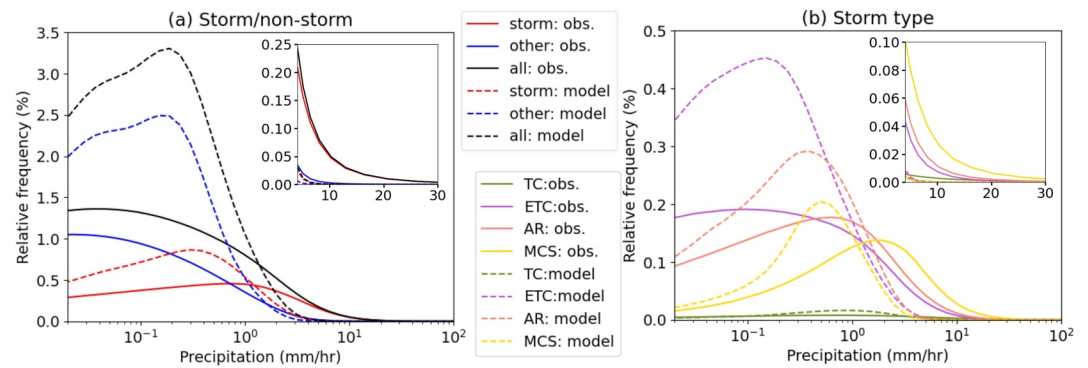
Figure 10. Hourly precipitation (mm hr^{-1}) distribution across time and space for 2011 from 1° grids over 60°S–60°N. Relative frequency represents the counts relative to (normalized by) the counts of all precipitation (sample number of black line). OBS (solid lines) are based on IMERG (OBS), and models (dash line) are based on E3SM Day 2 hindcasts. Small panels in the upper right corner focus on the high tails (4–30 mm hr^{-1}).

larger than 4 mm hr^{-1} (upper right panels in Figure 10b), OBS suggests the strongest contribution arises from MCSs, although the model rarely produces such heavy precipitation regardless of storm types.

We further examine whether extreme precipitation (in top 1% precipitation hours) and its partitioning by storm type can be simulated in the hindcasts in Figure 11. As expected from the precipitation PDFs, the 99th percentile of precipitation from E3SM hindcasts is much smaller than in OBS (Figures 11a and 11g). The globally averaged 99th percentile of precipitation is 1.3 mm hr^{-1} for the E3SM hindcasts and 2.9 mm hr^{-1} for the IMERG (OBS). For each storm type, the accumulated precipitation above the 99th percentile is considerably underestimated (Figures 11b–11e and 11h–11l). In particular, contributions from MCSs show strong disagreement with OBS, especially in the tropics (Figures 11e and 11k). This suggests that even with realistic initialization of the hindcasts, the model significantly underestimates the intensity of these top 1% precipitation events, especially for those associated with MCSs in the tropics. As a result, only 59.5% of the accumulated precipitation from these four storm types in E3SM hindcasts contribute to the extreme precipitation, compared to 81.9% in OBS (Figure S9 in Supporting Information S1).

We also evaluate the diurnal cycle of precipitation for different storm types (Figure 12). Generally, the amplitude of the diurnal cycle is underestimated (Figures 12d and 12h), which is largely attributed too little MCS precipitation (Figure 12e). Although the model still generates a land-ocean contrast in the diurnal phase in MCS precipitation, a later peak is found over ocean in the model (early afternoon peak in the model and early morning peak in OBS). The MCS precipitation phase over land is relatively better simulated compared to that over ocean. Similar to the results for multi-year averages in OBS in Figure 8, OBS phases of storm-associated precipitation from 2011 averages are distinct from other precipitation sources (earlier peak in other precipitation sources; Figures 12b and 12c). However, this distinction is not obvious in model results (Figures 12f and 12g). Unlike the afternoon peak over land for other precipitation sources in OBS (Figure 12c), the model typically peaks in the evening, which is closer to the peaks of MCS precipitation events. This suggests that the distinct features of larger and longer duration MCSs that separate them from smaller individual convective storms are not captured in the model, particularly over land. For other precipitation over the tropical ocean, the model agrees quite well with OBS on the midnight to early morning peak (Figures 12c and 12g). However, it should be noted that diurnal precipitation from E3SM version 2 was improved compared to version 1 due to the revised convective triggering scheme (Golaz et al., 2022; S. Xie et al., 2019).

Finally, we evaluate the precipitation structure of individual storm types. Figure 13 shows composites of precipitation for each storm type for OBS (blue shaded of Figure 13 top panels), hindcasts (red contours of top panels) and their differences (Figure 13 bottom panels). The composites are produced with TempestExtremes, by averaging surrounding fields centered on each feature center. The storm-centered precipitation fields are the results without masking (no storm boundaries) and prioritization mentioned in Section 2.3. A box of 21 × 21 grid points at 1° resolutions is centered at TC/ETC centers or centroid points for AR/MCS areal features within 50°S–50°N in 2011. For all storm types, model hindcasts underestimate precipitation intensity, especially for the peaks around the storm centers (Figure 13). The magnitude of the underestimated precipitation is especially large in the
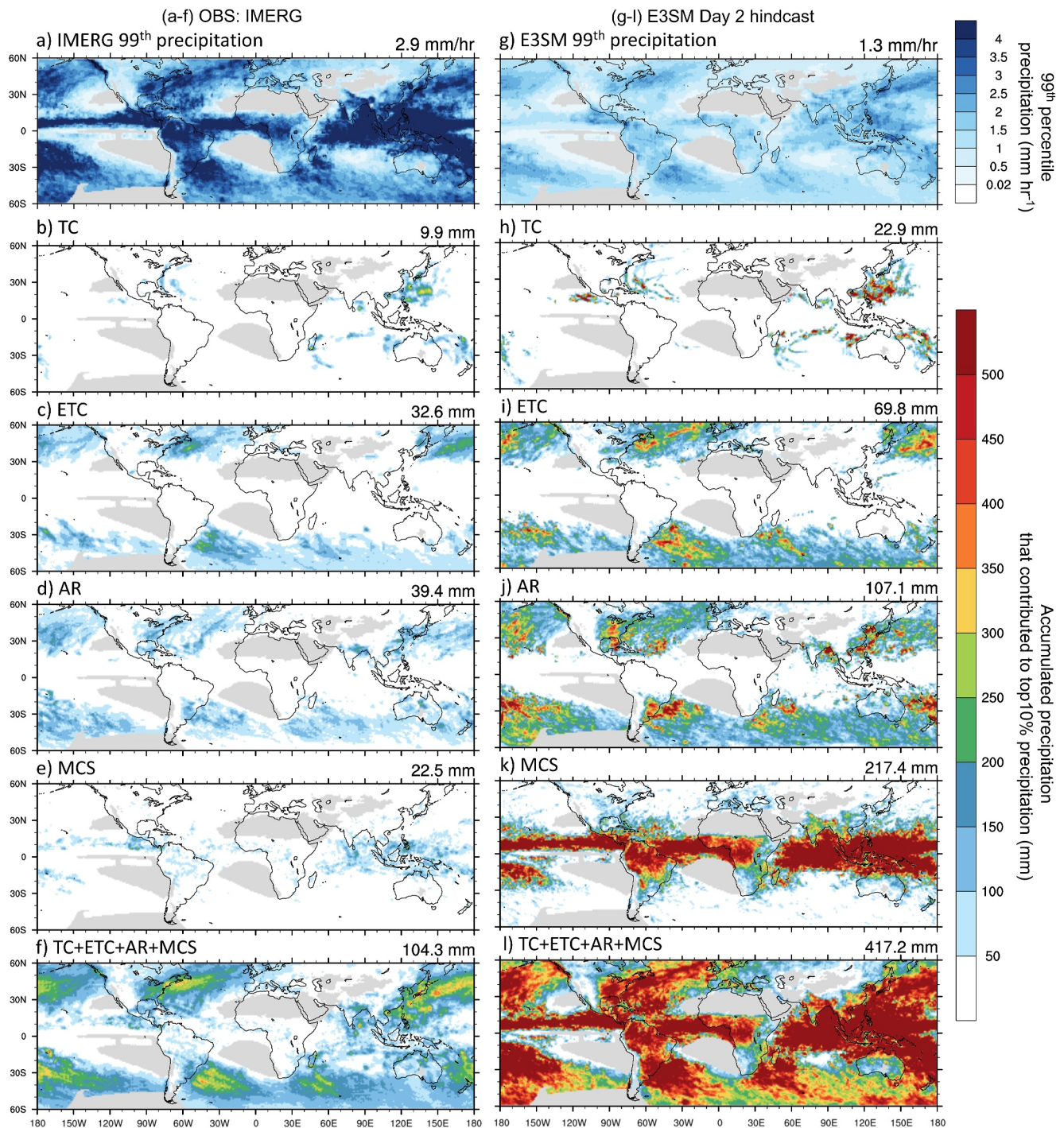
Figure 11. Comparison of extreme precipitation between IMERG (OBS) and E3SM hindcast. (a/g) 99th percentile values are based on hourly IMERG/E3SM precipitation in 2011. (b–f) Accumulated precipitation, which contribute to the top 1% precipitation hours from each storm types from IMERG (OBS), and (h–l) ones from E3SM Day 2 hindcast.

storm center compared to surrounding regions. Although the precipitation intensity is largely underestimated, the locations of the composited storm center do not shift, likely because of the coarse grid size and global averaging. However, further investigation is needed to understand whether the dynamics and propagation (e.g., location, size, intensity) of the individual storms are well simulated in models.
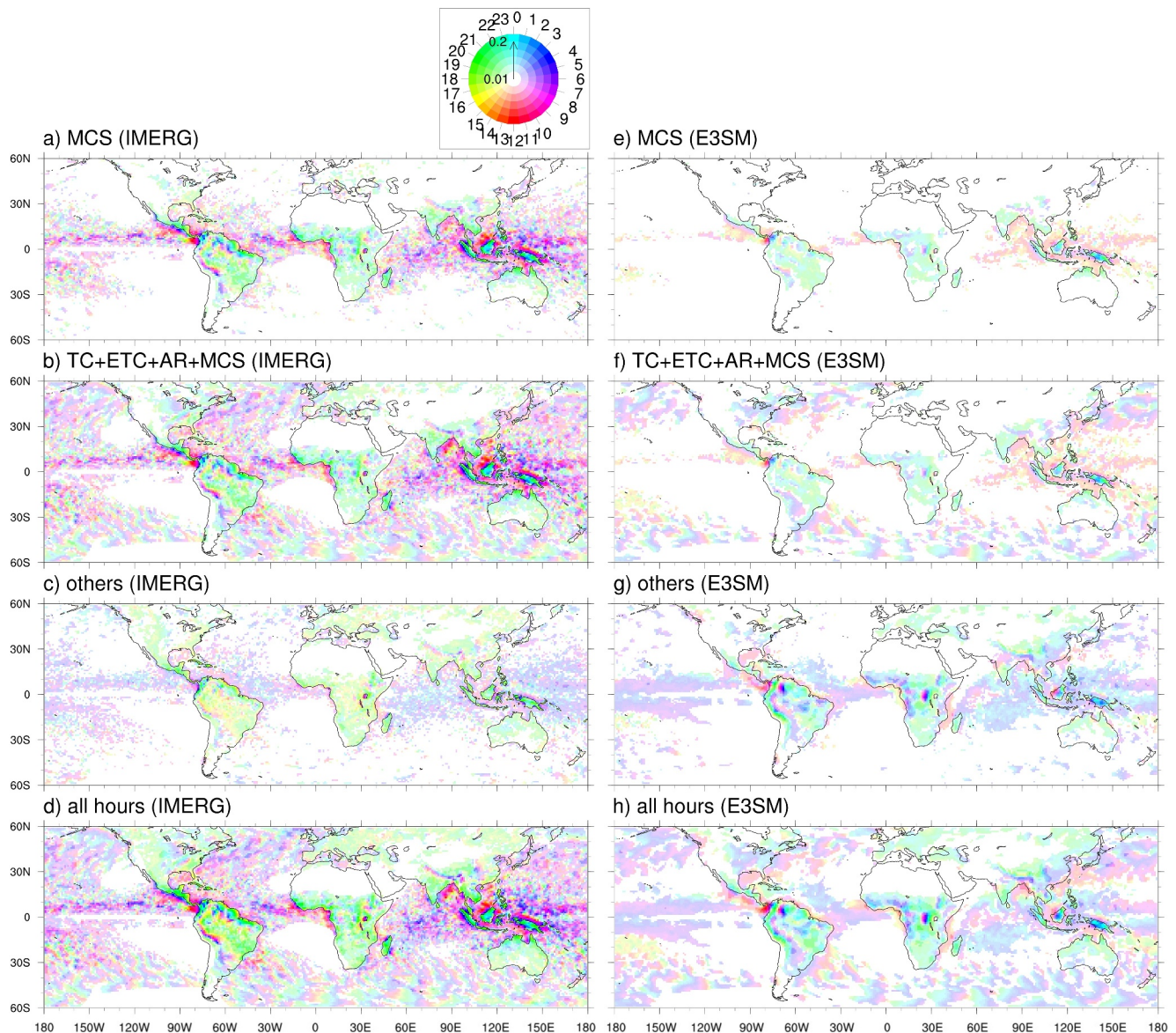
Figure 12. Composited diurnal cycle of precipitation in 2011. (left) IMERG OBS (right) E3SM Day 2 hindcast. The diurnal phase (shown as colors) is in local standard time, and the diurnal amplitude in mm hr^{-1} is shown as saturation. Magnitudes in panels (a–h) are all normalized by all hours, not the individual storm event hours.

4. Discussion

In this study, we perform a phenomena-based evaluation for E3SM short-range hindcasts using the same storm masks as OBS. Note that although the large-scale environment is still close to the initial ERA5 state, E3SM with low-resolution configuration alone cannot properly simulation the life cycle of all storms, especially for MCSs and TCs. Therefore, this also contributes to part of the underestimation of storm precipitation.

Conceptually different from hindcasts, feature tracking is expected to be done independently for free running ESM simulations, like those simulations from CMIP6. Therefore, it is worth examining how model resolution and output frequency affects the number of tracked features, if feature tracking is applied to other CMIP simulations. Here we resample ERA-5 data to different resolutions (Table 2) and apply the same TC tracking algorithms. We only examined TCs because we expect ETCs and ARs to be less sensitive to resolution, owing to their larger spatiotemporal scale, and noting that current free-running conventional ESMs (25–250 km) are too coarse to capture finer-scale MCSs (H.-Y. Ma et al., 2022). We apply two processing methods to upscale the data temporally: (a) we subsample the hourly data at the desired frequency (e.g., keep hourly data at 00z for daily
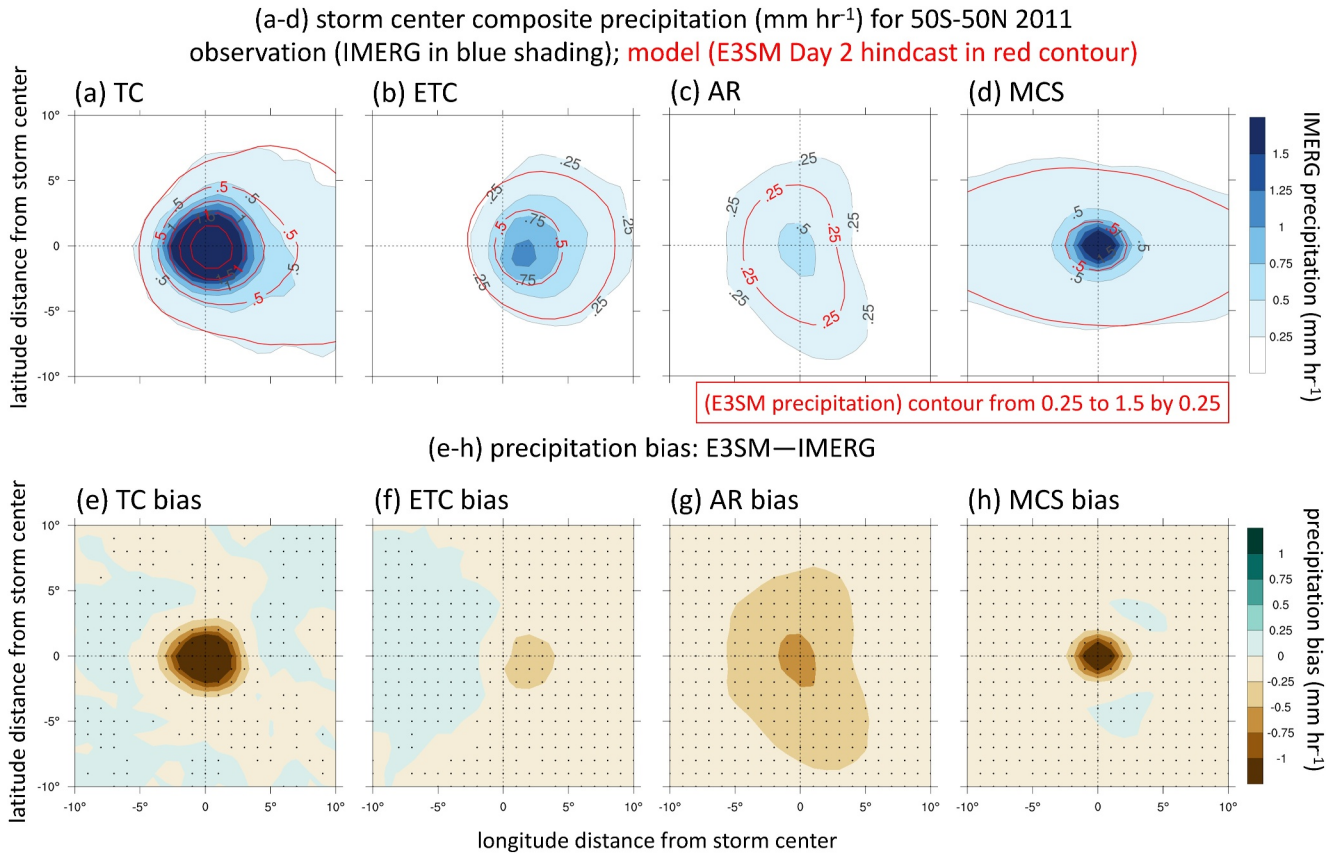
(a-d) storm center composite precipitation (mm hr⁻¹) for 50S-50N 2011
observation (IMERG in blue shading); model (E3SM Day 2 hindcast in red contour)

(E3SM precipitation) contour from 0.25 to 1.5 by 0.25

(e-h) precipitation bias: E3SM—IMERG

Figure 13. Comparison of modeled (red contour, for E3SM hindcast Day 2) and OBS (blue colored shading, for IMERG) storm precipitation (mm hr⁻¹) at top and their differences at bottom. Precipitation is composited with center of the storm system. Centers of atmospheric rivers (ARs) and mesoscale convective systems are defined as the geometric centroid of the detected regions. Composites are the based on hourly data in 2011 with storm centers occurring in 50°S–50°N. These results do not include the masking and prioritizing method mentioned in Section 2.4. Snapshots of 21 × 21 grids in 1° resolutions are shown. Dots mark the regions where are statistically significant at 95% level with determined by a t-test using variances of hourly snapshots. Results of different AR composite methods are shown in Figure S10 in Supporting Information S1.

Table 2
Comparison of Tracked Tropical Cyclone Numbers in 2011 Globally Using Inputs of Different Spatiotemporal Resolutions

Temporal resolution	Sampling (filtering) or averaging from hourly data	Spatial resolution (°)	Tracked TC numbers
Hourly	None	0.25	97
Hourly	None	0.5	87 (−10%)
Hourly	None	1.0	79 (−19%)
3-Hourly	Sampling	0.25	91 (−6%)
6-Hourly	Sampling	0.25	85 (−12%)
Daily	Sampling	0.25	76 (−22%)
Daily	Sampling	0.5	75 (−23%)
Daily	Sampling	1.0	73 (−25%)
Daily	Averaging	0.25	56 (−42%)
Daily	Averaging	0.50	53 (−45%)
Daily	Averaging	1.0	51 (−47%)

Note. Original input data are ERA5 at hourly and 0.25°, and then upscale to different resolutions.

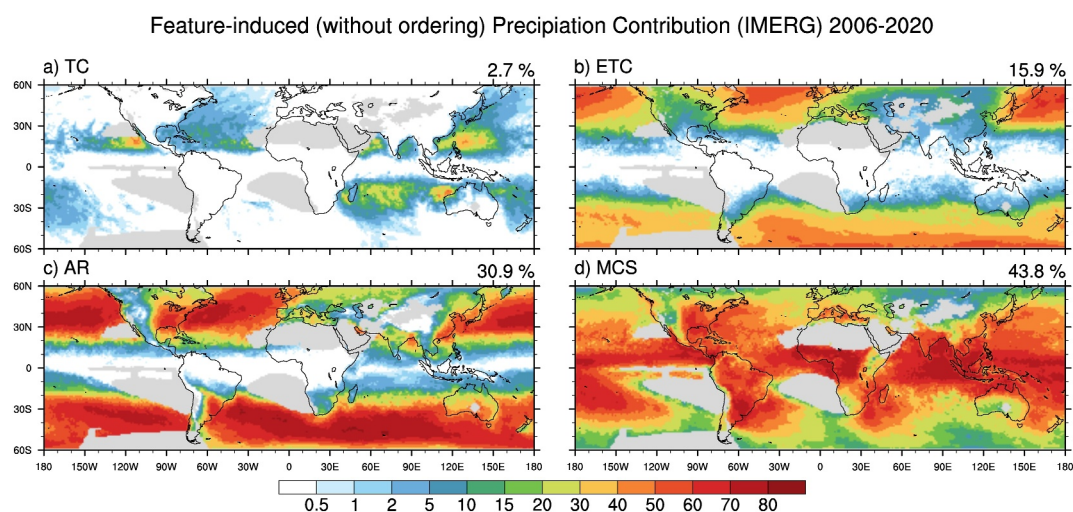Feature-induced (without ordering) Precipiation Contribution (IMERG) 2006-2020

Figure 14. Precipitation contribution (%, relative to the total precipitation of each grid cell) based on IMERG for 2006–2020 without prioritization/ordering of storm types. The overlapping results are present in Figure S11 in Supporting Information S1.

sampling), or (b) we average all hours of the sample periods (e.g., average 24 hr). These two different approaches imitate two types of ESM output strategies: averaging or instantaneous fields. Temporal averaging smooths the fields and diminishes the dynamic evaluation within the time frame, while simply sampling the data retains the original patterns. We also coarsen the 0.25° resolution data to 0.5° and 1.0° resolutions. Table 2 shows that the number of global TCs drops with coarser temporal or spatial resolutions by 6%–47%, which indicates that feature tracking is sensitive to the spatiotemporal resolutions of input data. More interestingly, temporal resolution (hourly, 3-hourly, 6-hourly, and daily) has larger impact than spatial resolution (0.25°, 0.5°, and 1.0°). We also find that subsampling data has less impact than averaging. Note that changing the resolution of the model configuration is different from remapping the data as done here. However, this exercise can still provide guidance on the limitations of coarse resolutions in future studies.

In addition to feature tracking, we apply prioritization/ordering to avoid overlayed storm types. In reality, these storm types sometimes occur simultaneously, for example, some ARs are the heavy moisture transport corresponding to the cold fronts of ETCs. MCSs can also overlap with all other storm types (TCs, ETCs, and ARs; Feng, Leung, et al., 2021; Feng, Song, et al., 2021). When setting the order of prioritization, we carefully consider the spatiotemporal scales, accuracy of tracking, and rigorousness of each definition across different storm types (e.g., Prein et al., 2023; Zhao, 2022). Here we contrast the results without the prioritization ordering procedure. Figure 14 shows the precipitation contributions similar as Figure 4 but without prioritization/ordering, and Figure S10 in Supporting Information S1 shows the precipitation contribution of each co-occurring features to total precipitation. The comparisons show that prioritization/ordering leads to lower AR- and MCS- associated precipitation. Lower AR precipitation is caused by removing ETC/AR overlapping along the storm tracks in mid-latitude oceans. The global average MCS precipitation contribution before and after prioritization is 43.8% and 26.7%, respectively. The reduction is mainly in the mid-latitude ocean and some parts of land, including the Eastern US and a small portion of Southeastern South America, in part due to co-occurring of ARs and MCSs (Figure S10f in Supporting Information S1). More detail study of interactions and co-occurrences of different storm types are done by Prein et al. (2023).

Some weak storms are not expected to be tracked and are classified as other precipitation sources ("others"). "Others" can also come from weak versions of tracked features. For example, AR-related precipitation over the continental west coasts is sometimes not associated with the tracked ARs, and it might be due to the rapid IVT decay at AR landfalls (Rutz et al., 2015). Future studies of redesigning tracking algorithms could include more surrounding precipitation. Nevertheless, precipitation characteristics from "others" and storms (TC/ETC/AR/ MCS) have clear distinctions in their distribution (Figures 6 and 7) and diurnal cycles (Figure 8), which suggests substantial contributions of local unorganized convections to "others."

5. Summary and Conclusions

In this study, we establish a global observational database of tracks for four major heavy-rain storm systems: TCs, ETCs, ARs, and MCSs. The global (60°S–60°N) data set is from 2006 to 2020 at high spatial and temporal resolutions (0.25° and hourly). We document the characteristics of storm-associated precipitation using OBS, and also evaluate the performance of short-term hindcasts from E3SM in simulating these storm systems.

The OBS analysis shows that TC/ETC/AR/MCS together account for 51% of rain hours and 67% of total global precipitation amounts annually. These four storm types have strong seasonality and location dependencies and play a crucial role in extreme precipitation, especially in the midlatitudes. On average, TC/ETC/AR/MCS contribute to 82% of the heaviest precipitation events (those above 99th hourly percentile). Among the storm types, the contribution of MCS to precipitation extremes is the largest, especially in the tropics, in agreement with previous findings (Feng, Leung, et al., 2021; Prein et al., 2023; Zhao, 2022). We also find that MCS-associated precipitation has a pronounced diurnal cycles and a strong land-ocean contrast that mostly explains the diurnal cycle in tropics.

The present study also provides a new and unique approach for model diagnostics by focusing on storm-associated precipitation, demonstrated using climate model short-term hindcasts. We find that E3SM at 1° spatial resolution significantly underestimates storm-associated precipitation intensity but overestimates other precipitation sources. Hourly precipitation PDFs suggest that the four storm types account for most of the heavy precipitation, which model is largely underestimated. The global mean 99th percentile precipitation amount from E3SM is much smaller than that found in OBS, especially over the tropics where MCS precipitation is significantly underestimated. The diurnal cycle phase and amplitude of precipitation for different storm types are also evaluated. E3SM generally underestimates the amplitude of the diurnal cycle and simulates incorrect phases especially for MCSs in the tropics and other precipitation sources over land.

For the hindcast evaluation, we find that Day 2 simulations largely underestimated precipitation in MCS regions, which might be due to various reasons. First, the model resolution used here (1°) is not fine enough to simulate most of the MCSs though initialized by reanalysis. Therefore, we plan to apply this framework to higher resolution hindcasts (i.e., 0.25° or finer) in the future. Second, we hypothesize most of the underestimated MCS precipitation is partly due to discrepancies of short-lived MCSs (i.e., lifetime shorter than 24 hr). Future work is needed to understand how MCS characteristics affect the predictability.

As ESMs continually move toward finer resolutions, this storm-based approach is especially suitable for phenomenon-based evaluation, leading to a better process-level understanding for intense and extreme precipitation events. This evaluation framework can also be applied to a variety of applications, including feature detection, sub-seasonal to seasonal forecasts, and climate change effects on storm-associated precipitation characteristics.

Data Availability Statement

All data sets used for this study are publicly available. We obtained ERA-5 hourly reanalysis from https://doi.org/10.24381/cds.adbb2d47 and https://doi.org/10.24381/cds.bd0915c6 (Hersbach et al., 2018), IMERG from https://doi.org/10.5067/GPM/IMERG/3B-HH/06 (Huffman et al., 2019), and CMORPH from https://www.ncei.noaa.gov/products/climate-data-records/precipitation-cmorph (P. Xie et al., 2019). Tempestextremes feature tracking software is available at https://github.com/ClimateGlobalChange/tempestextremes. PyFLEXTRKR is available at https://github.com/FlexTRKR/PyFLEXTRKR. The U.S. DOE E3SM v2.0 model is available at https://doi.org/10.11578/E3SM/dc.20210927.1 (E3SM Project, DOE, 2021). Data sets used in this study are accessible via NERSC Science Gateway portal at: https://portal.nersc.gov/archive/home/w/wu59/www/2024JGR. The code generated in this study can be provided upon request to the corresponding author.

References

Ayat, H., Evans, J. P., Sherwood, S., & Behrangi, A. (2020). Are storm characteristics the same when viewed using merged surface radars or a merged satellite product? *Journal of Hydrometeorology*, *22*(1), 43–62. https://doi.org/10.1175/JHM-D-20-0187.1

Caldwell, P. M., Mametjanov, A., Tang, Q., Van Roekel, L. P., Golaz, J.-C., Lin, W., et al. (2019). The DOE E3SM coupled model version 1: Description and results at high resolution. *Journal of Advances in Modeling Earth Systems*, *11*(12), 4095–4146. https://doi.org/10.1029/2019MS001870

Chen, D., Dai, A., & Hall, A. (2021). The convective-to-total precipitation ratio and the "drizzling" bias in climate models. *Journal of Geophysical Research: Atmospheres*, *126*(16), e2020JD034198. https://doi.org/10.1029/2020JD034198

Cui, W., Dong, X., Xi, B., Feng, Z., & Fan, J. (2020). Can the GPM IMERG final product accurately represent MCSs' precipitation characteristics over the central and eastern United States? *Journal of Hydrometeorology*, *21*(1), 39–57. https://doi.org/10.1175/JHM-D-19-0123.1

Dai, A. (2006). Precipitation characteristics in eighteen coupled climate models. *Journal of Climate*, *19*(18), 4605–4630. https://doi.org/10.1175/JCLI3884.1

Derin, Y., Kirstetter, P.-E., Brauer, N., Gourley, J. J., & Wang, J. (2022). Evaluation of IMERG satellite precipitation over the land–coast–ocean continuum. Part II: Quantification. *Journal of Hydrometeorology*, *23*(8), 1297–1314. https://doi.org/10.1175/JHM-D-21-0234.1

E3SM Project, DOE. (2021). Energy Exascale Earth system model v2.0 [Software]. Retrieved from https://github.com/E3SM-Project/E3SM/releases/tag/v2.0.0

Eyring, V., Bony, S., Meehl, G. A., Senior, C. A., Stevens, B., Stouffer, R. J., & Taylor, K. E. (2016). Overview of the coupled model inter-comparison project phase 6 (CMIP6) experimental design and organization. *Geoscientific Model Development*, *9*(5), 1937–1958. https://doi.org/10.5194/gmd-9-1937-2016

Feng, Z., Hardin, J., Barnes, H. C., Li, J., Leung, L. R., Varble, A., & Zhang, Z. (2023). PyFLEXTRKR: A flexible feature tracking Python software for convective cloud analysis. *Geoscientific Model Development*, *16*(10), 2753–2776. https://doi.org/10.5194/gmd-16-2753-2023

Feng, Z., Houze, R. A., Leung, L. R., Song, F., Hardin, J. C., Wang, J., et al. (2019). Spatiotemporal characteristics and large-scale environments of mesoscale convective systems east of the Rocky mountains. *Journal of Climate*, *32*(21), 7303–7328. https://doi.org/10.1175/JCLI-D-19-0137.1

Feng, Z., Leung, L. R., Houze, R. A., Jr., Hagos, S., Hardin, J., Yang, Q., et al. (2018). Structure and evolution of mesoscale convective systems: Sensitivity to cloud microphysics in convection-permitting simulations over the United States. *Journal of Advances in Modeling Earth Systems*, *10*(7), 1470–1494. https://doi.org/10.1029/2018MS001305

Feng, Z., Leung, L. R., Liu, N., Wang, J., Houze Jr, R. A., Li, J., et al. (2021). A global high-resolution mesoscale convective system database using satellite-derived cloud tops, surface precipitation, and tracking. *Journal of Geophysical Research: Atmospheres*, *126*(8), e2020JD034202. https://doi.org/10.1029/2020JD034202

Feng, Z., Song, F., Sakaguchi, K., & Leung, L. R. (2021). Evaluation of mesoscale convective systems in climate simulations: Methodological development and results from MPAS-CAM over the United States. *Journal of Climate*, *34*(7), 2611–2633. https://doi.org/10.1175/JCLI-D-20-0136.1

Golaz, J.-C., Van Roekel, L. P., Zheng, X., Roberts, A. F., Wolfe, J. D., Lin, W., et al. (2022). The DOE E3SM model version 2: Overview of the physical model and initial model evaluation. *Journal of Advances in Modeling Earth Systems*, *14*(12), e2022MS003156. https://doi.org/10.1029/2022MS003156

Hawcroft, M. K., Shaffrey, L. C., Hodges, K. I., & Dacre, H. F. (2012). How much Northern Hemisphere precipitation is associated with extratropical cyclones? *Geophysical Research Letters*, *39*(24), L24809. https://doi.org/10.1029/2012GL053866

Hersbach, H., Bell, B., Berrisford, P., Biavati, G., Horányi, A., Muñoz Sabater, J., et al. (2018). ERA5 hourly data on single levels from 1959 to present [Dataset]. *Copernicus Climate Change Service (C3S) Climate Data Store (CDS)*. https://doi.org/10.24381/cds.adbb2d47

Hersbach, H., Bell, B., Berrisford, P., Hirahara, S., Horányi, A., Muñoz-Sabater, J., et al. (2020). The ERA5 global reanalysis. *Quarterly Journal of the Royal Meteorological Society*, *146*(730), 1999–2049. https://doi.org/10.1002/qj.3803

Huffman, G. J., Bolvin, D. T., Nelkin, E. J., Stocker, E. F., & Tan, J. (2020). V06 IMERG release notes. Retrieved from https://docserver.gesdisc.eosdis.nasa.gov/public/project/GPM/IMERG_V06_release_notes.pdf

Huffman, G. J., Stocker, E. F., Bolvin, D. T., Nelkin, E. J., & Tan, J. (2019). GPM IMERG final precipitation L3 half hourly 0.1 degree x 0.1 degree V06 [Dataset]. *Goddard Earth Sciences Data and Information Services Center (GES DISC)*. https://doi.org/10.5067/GPM/IMERG/3B-HH/06

Janowiak, J. E., Joyce, R. J., & Yarosh, Y. (2001). A real-time global half-hourly pixel-resolution infrared dataset and its applications. *Bulletin of the American Meteorological Society*, *82*(2), 205–218. https://doi.org/10.1175/1520-0477(2001)082<0205:ARTGHH>2.3.CO;2

Knapp, K. R., & Kruk, M. C. (2010). Quantifying interagency differences in tropical cyclone best-track wind speed estimates. *Monthly Weather Review*, *138*(4), 1459–1473. https://doi.org/10.1175/2009MWR3123.1

Kooperman, G. J., Akinsanola, A. A., Hannah, W. M., Pendergrass, A. G., & Reed, K. A. (2022). Assessing two approaches for enhancing the range of simulated scales in the E3SMv1 and the impact on the character of hourly US precipitation. *Geophysical Research Letters*, *49*(4), e2021GL096717. https://doi.org/10.1029/2021GL096717

Leung, L. R., Boos, W. R., Catto, J. L., DeMott, C., Martin, G. M., Neelin, J. D., et al. (2022). Exploratory precipitation metrics: Spatiotemporal characteristics, process-oriented, and phenomena-based. *Journal of Climate*, *I*(12), 1–55. https://doi.org/10.1175/JCLI-D-21-0590.1

Ma, H.-Y., Chuang, C. C., Klein, S. A., Lo, M.-H., Zhang, Y., Xie, S., et al. (2015). An improved hindcast approach for evaluation and diagnosis of physical processes in global climate models. *Journal of Advances in Modeling Earth Systems*, *7*(4), 1810–1827. https://doi.org/10.1002/2015MS000490

Ma, H.-Y., Klein, S. A., Lee, J., Ahn, M.-S., Tao, C., & Gleckler, P. J. (2022). Superior daily and sub-daily precipitation statistics for intense and long-lived storms in global storm-resolving models. *Geophysical Research Letters*, *49*(8), e2021GL096759. https://doi.org/10.1029/2021GL096759

Ma, H.-Y., Xie, S., Boyle, J. S., Klein, S. A., & Zhang, Y. (2013). Metrics and diagnostics for precipitation-related processes in climate model short-range hindcasts. *Journal of Climate*, *26*(5), 1516–1534. https://doi.org/10.1175/JCLI-D-12-00235.1

Ma, H.-Y., Zhou, C., Zhang, Y., Klein, S. A., Zelinka, M. D., Zheng, X., et al. (2021). A multi-year short-range hindcast experiment with CESM1 for evaluating climate model moist processes from diurnal to interannual timescales. *Geoscientific Model Development*, *14*(1), 73–90. https://doi.org/10.5194/gmd-14-73-2021

Ma, W., Chen, G., Guan, B., Shields, C. A., Tian, B., & Yanez, E. (2023). Evaluating the representations of atmospheric rivers and their associated precipitation in reanalyses with satellite observations. *Journal of Geophysical Research: Atmospheres*, *128*(22), e2023JD038937. https://doi.org/10.1029/2023JD038937

McClenny, E. E., Ullrich, P. A., & Grotjahn, R. (2020). Sensitivity of atmospheric river vapor transport and precipitation to uniform sea surface temperature increases. *Journal of Geophysical Research: Atmospheres*, *125*(21), e2020JD033421. https://doi.org/10.1029/2020JD033421

Nesbitt, S. W., & Zipser, E. J. (2003). The diurnal cycle of rainfall and convective intensity according to three years of TRMM measurements. *Journal of Climate*, *16*(10), 1456–1475. https://doi.org/10.1175/1520-0442(2003)016<1456:TDCORA>2.0.CO;2

NOAA National Centers for Environmental Information. (2023). Monthly national climate report for January 2023. Retrieved from https://www.ncei.noaa.gov/access/monitoring/monthly-report/national/202301

Prein, A. F., Mooney, P. A., & Done, J. M. (2023). The multi-scale interactions of atmospheric phenomenon in mean and extreme precipitation. *Earth's Future*, *11*, e2023EF003534. https://doi.org/10.1029/2023EF003534

Prein, A. F., Rasmussen, R. M., Wang, D., & Giangrande, S. E. (2021). Sensitivity of organized convective storms to model grid spacing in current and future climates. *Philosophical Transactions of the Royal Society A: Mathematical, Physical & Engineering Sciences*, *379*(2195), 20190546. https://doi.org/10.1098/rsta.2019.0546

Reed, K. A., Stansfield, A. M., Hsu, W.-C., Kooperman, G. J., Akinsanola, A. A., Hannah, W. M., et al. (2023). Evaluating the simulation of CONUS precipitation by storm type in E3SM. *Geophysical Research Letters*, *50*(12), e2022GL102409. https://doi.org/10.1029/2022GL102409

Reynolds, R. W., Rayner, N. A., Smith, T. M., Stokes, D. C., & Wang, W. (2002). An improved in situ and satellite SST analysis for climate. *Journal of Climate*, *15*(13), 1609–1625. https://doi.org/10.1175/1520-0442(2002)015<1609:aiisas>2.0.co;2

Rutz, J. J., Steenburgh, W. J., & Ralph, F. M. (2015). The Inland penetration of atmospheric rivers over western North America: A Lagrangian analysis. *Monthly Weather Review*, *143*(5), 1924–1944. https://doi.org/10.1175/MWR-D-14-00288.1

Schulzweida, U. (2023). CDO user guide (2.3.0). [Software]. *Zenodo*. https://doi.org/10.5281/zenodo.10020800

Shields, C. A., & Kiehl, J. T. (2016). Atmospheric river landfall-latitude changes in future climate simulations. *Geophysical Research Letters*, *43*(16), 8775–8782. https://doi.org/10.1002/2016GL070470

Stansfield, A. M., Reed, K. A., Zarzycki, C. M., Ullrich, P. A., & Chavas, D. R. (2020). Assessing tropical cyclones' contribution to precipitation over the eastern United States and sensitivity to the variable-resolution domain extent. *Journal of Hydrometeorology*, *21*(7), 1425–1445. https://doi.org/10.1175/JHM-D-19-0240.1

Stevens, B., Satoh, M., Auger, L., Biercamp, J., Bretherton, C. S., Chen, X., et al. (2019). DYAMOND: The DYnamics of the atmospheric general circulation modeled on non-hydrostatic domains. *Progress in Earth and Planetary Science*, *6*(1), 61. https://doi.org/10.1186/s40645-019-0304-z

Sun, Y., Solomon, S., Dai, A., & Portmann, R. W. (2006). How often does it rain? *Journal of Climate*, *19*(6), 916–934. https://doi.org/10.1175/JCLI3672.1

Tao, C., Xie, S., Tang, S., Lee, J., Ma, H.-Y., Zhang, C., & Lin, W. (2022). Diurnal cycle of precipitation over global monsoon systems in CMIP6 simulations. *Climate Dynamics*, *60*(11–12), 3947–3968. https://doi.org/10.1007/s00382-022-06546-0

Ullrich, P. A. (2022). TempestExtremes GitHub repository [Software]. *GitHub*. https://github.com/ClimateGlobalChange/tempestextremes

Ullrich, P. A., & Zarzycki, C. M. (2017). TempestExtremes: A framework for scale-insensitive pointwise feature tracking on unstructured grids. *Geoscientific Model Development*, *10*(3), 1069–1090. https://doi.org/10.5194/gmd-10-1069-2017

Ullrich, P. A., Zarzycki, C. M., McClenny, E. E., Pinheiro, M. C., Stansfield, A. M., & Reed, K. A. (2021). TempestExtremes v2.1: A community framework for feature detection, tracking, and analysis in large datasets. *Geoscientific Model Development*, *14*(8), 5023–5048. https://doi.org/10.5194/gmd-14-5023-2021

Wang, J., Wolff, D. B., Tan, J., Marks, D. A., Pippitt, J. L., & Huffman, G. J. (2022). Validation of IMERG oceanic precipitation over Kwajalein. *Remote Sensing*, *14*(15), 15. https://doi.org/10.3390/rs14153753

Xie, P., Joyce, R., Wu, S., Yoo, S.-H., Yarosh, Y., Sun, F., et al. (2019). NOAA climate data record (CDR) of CPC morphing technique (CMORPH) high resolution global precipitation estimates, version 1 (0.25-degree hourly) [Dataset]. *NOAA National Centers for Environmental Information*. https://doi.org/10.25921/w9va-q159

Xie, S., Wang, Y.-C., Lin, W., Ma, H.-Y., Tang, Q., Tang, S., et al. (2019). Improved diurnal cycle of precipitation in E3SM with a revised convective triggering function. *Journal of Advances in Modeling Earth Systems*, *11*(7), 2290–2310. https://doi.org/10.1029/2019MS001702

Zarzycki, C. M. (2018). Projecting changes in societally impactful northeastern U.S. Snowstorms. *Geophysical Research Letters*, *45*(21), 12067–12075. https://doi.org/10.1029/2018GL079820

Zarzycki, C. M., Thatcher, D. R., & Jablonowski, C. (2017). Objective tropical cyclone extratropical transition detection in high-resolution reanalysis and climate model data. *Journal of Advances in Modeling Earth Systems*, *9*(1), 130–148. https://doi.org/10.1002/2016MS000775

Zarzycki, C. M., & Ullrich, P. A. (2017). Assessing sensitivities in algorithmic detection of tropical cyclones in climate data. *Geophysical Research Letters*, *44*(2), 1141–1149. https://doi.org/10.1002/2016GL071606

Zarzycki, C. M., Ullrich, P. A., & Reed, K. A. (2021). Metrics for evaluating tropical cyclones in climate data. *Journal of Applied Meteorology and Climatology*, *60*(5), 643–660. https://doi.org/10.1175/JAMC-D-20-0149.1

Zhao, M. (2020). Simulations of atmospheric rivers, their variability, and response to global warming using GFDL's new high-resolution general circulation model. *Journal of Climate*, *33*(23), 10287–10303. https://doi.org/10.1175/JCLI-D-20-0241.1

Zhao, M. (2022). A study of AR-TS-and MCS-associated precipitation and extreme precipitation in present and warmer climates. *Journal of Climate*, *35*(2), 479–497. https://doi.org/10.1175/JCLI-D-21-0145.1

Zhao, M., Held, I. M., Lin, S.-J., & Vecchi, G. A. (2009). Simulations of global hurricane climatology, interannual variability, and response to global warming using a 50-km resolution GCM. *Journal of Climate*, *22*(24), 6653–6678. https://doi.org/10.1175/2009JCLI3049.1